JACS
JOURNAL OF THE AMERICAN CHEMICAL SOCIETY
pubs.acs.org/JACS
Article

# Effect of Strong Intermolecular Interaction in 2D Inorganic Molecular Crystals

Xin Feng,[⊥] Xingliang Peng,[⊥] Baixin Peng, Zexin Li, Wentao Huang, Sijie Yang, Ke Pei, Zongdong Sun, Fuqiang Huang, Huiqiao Li, Zhigang Shuai,[*] and Tianyou Zhai[*]

Cite This: *J. Am. Chem. Soc.* 2021, 143, 20192−20201

Read Online

ACCESS | Metrics & More | Article Recommendations | Supporting Information

**ABSTRACT:** Strong intermolecular interactions in 2D organic molecular crystals arising from $\pi-\pi$ stacking have been widely explored to achieve high thermal stability, high carrier mobility, and novel physical properties, which have already produced phenomenal progress. However, strong intermolecular interactions in 2D inorganic molecular crystals (2DIMCs) have rarely been investigated, severely limiting both the fundamental research in molecular physics and the potential applications of 2DIMCs for optoelectronics. Here, the effect of strong intermolecular interactions induced by unique short intermolecular Se−Se and P−Se contacts in 2D $\alpha$-$P_4Se_3$ nanoflakes is reported. On the basis of theoretical calculations of the charge density distribution and an analysis of the thermal expansion and plastic−crystal transition, the physical picture of strong intermolecular interactions can be elucidated as a higher charge density between adjacent $P_4Se_3$ molecules, arising from an orderly and close packing of $P_4Se_3$ molecules. More importantly, encouraged by the strong intermolecular coupling, the in-plane mobility of $\alpha$-$P_4Se_3$ nanoflakes is first calculated with a quantum nuclear tunneling model, and a competitive hole mobility of 0.4 cm$^2$ V$^{-1}$ s$^{-1}$ is obtained. Our work sheds new light on the intermolecular interactions in 2D inorganic molecular crystals and is highly significant for promoting the development of molecular physics and optoelectronics.

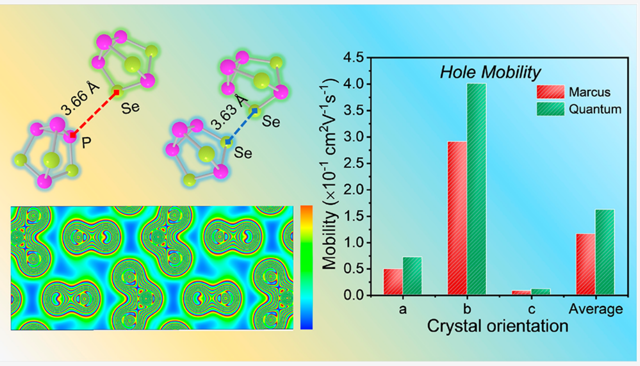

## ■ INTRODUCTION

2D molecular crystals (2DMCs) have had a tremendous effect on electronics and optoelectronics with their specific advantages of intrinsic flexibility, molecular diversity, low-cost processing, and tunable properties.[1−4] For 2DMCs, the intermolecular coupling is usually expected to be as strong as possible for the purpose of improving stability and obtaining high carrier mobility.[5−7] To date, strong intermolecular interactions in 2D organic crystals arising from $\pi-\pi$ stacking have been widely explored;[8−11] however, strong intermolecular interactions in 2D inorganic molecular crystals (2DIMCs) have rarely been investigated, and the few existing reports exclusively focused on hydrogen bonding.[12,13] The lack of understanding of strong intermolecular interactions in 2DIMCs has thus been greatly hindering the development of molecular physics and related optoelectronics. Though it is known that strong intermolecular interactions are always accompanied by a crystallographic feature, i.e. unusually short interatomic distances between molecules,[6,8,9,12] unfortunately, the effect and origin of that have rarely been demonstrated clearly.[14,15] What is more, it is still highly challenging to obtain 2DIMCs because the anisotropic intermolecular interactions usually drive molecules to crystallize into 1D rods, which is unsatisfactory for large-scale processing, miniaturization, and integration for micronano devices based on 2DIMCs.[16−18] Therefore, apart from hydrogen bonding, the study of strong intermolecular interactions in 2DIMCs is of great significance for extending the understanding of intermolecular interactions as well as promoting the potential applications of 2DIMCs in optoelectronics.

Herein, we report the effect of strong intermolecular interaction in 2D $\alpha$-$P_4Se_3$ nanoflakes synthesized by drop-casting. The unique short intermolecular Se−Se and P−Se contacts in $\alpha$-$P_4Se_3$ nanoflakes are demonstrated via single-crystal X-ray diffraction (SC-XRD), and the strong intermolecular interaction induced by that is confirmed by X-ray photoelectron spectroscopy (XPS), temperature-dependent Raman spectra, and absorption spectra. With theoretical calculations of the charge density distribution and charge transfer integrals, the nature and strength of this strong intermolecular coupling are revealed. Motivated by the strong

**Received:** August 2, 2021
**Published:** November 15, 2021

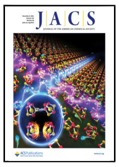

https://doi.org/10.1021/jacs.1c08030

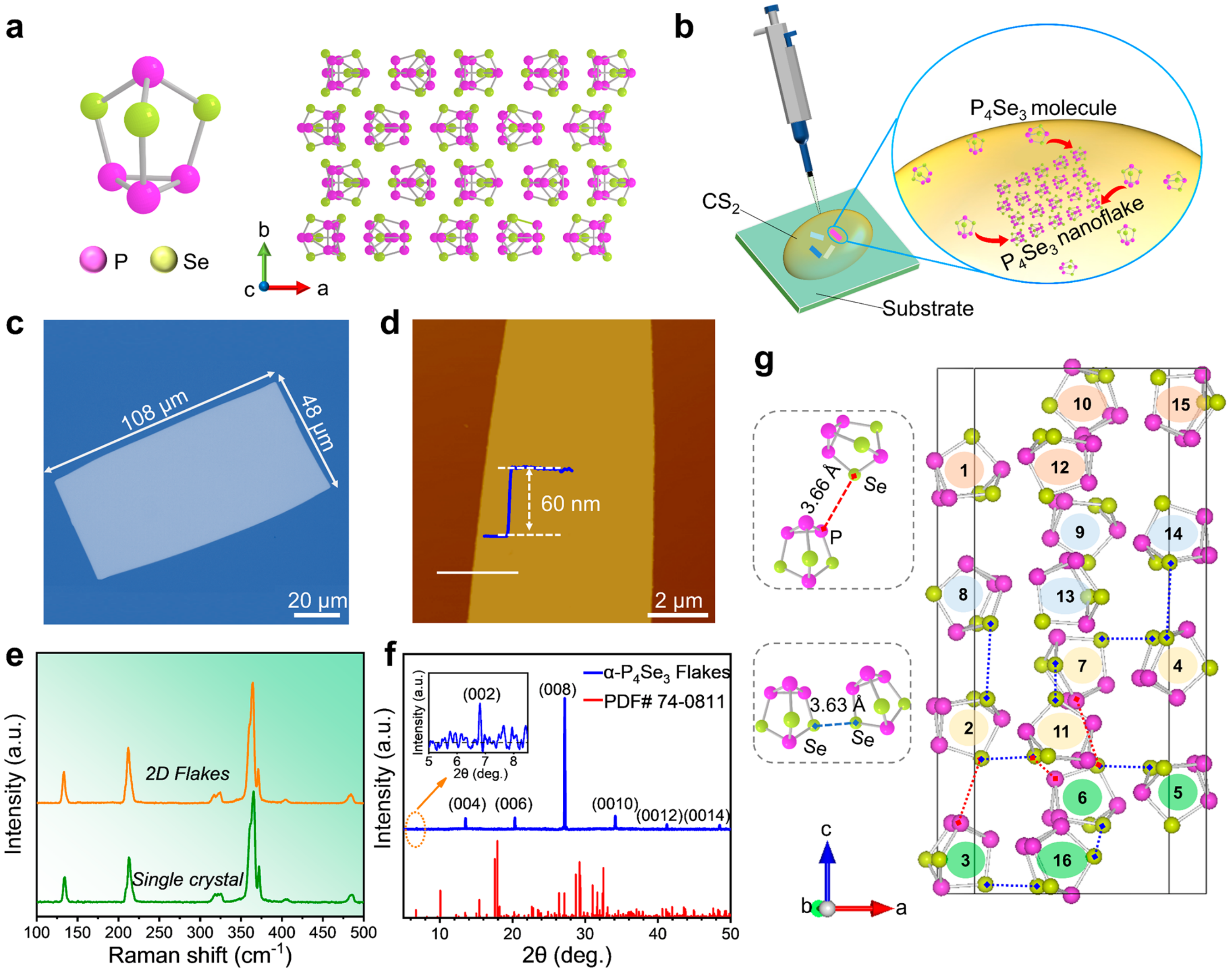

**Figure 1.** Growth and characterization of 2D $P_4Se_3$ nanoflakes. (a) A single $P_4Se_3$ molecule and a crystal structure diagram of $\alpha$-$P_4Se_3$. (b) Schematic diagram of the drop-casting growth process for 2D $P_4Se_3$ nanoflakes. (c) Optical image of an as-synthesized 2D $P_4Se_3$ nanoflake. (d) AFM image and height profile of the thinnest sample that we obtained. (e) Raman spectra of the 2D $P_4Se_3$ nanoflakes and $\alpha$-$P_4Se_3$ single crystal. (f) XRD pattern of the as-grown 2D $P_4Se_3$ nanoflakes. (g) Crystal structure of $\alpha$-$P_4Se_3$ determined from a single $P_4Se_3$ nanoflake and the unusually short interatomic distance that we observed between different molecules. The unusually short Se···Se and P···Se intermolecular contacts are depicted with blue and red dotted lines, respectively.

intermolecular coupling, we first calculated the in-plane mobility of 2DIMCs with a quantum nuclear tunneling model and obtained a competitive hole mobility of 0.4 $cm^2\ V^{-1}\ s^{-1}$. Moreover, we further demonstrate the photoelectric response of 2D $\alpha$-$P_4Se_3$ nanoflakes. Through analyzing the thermal expansion and plastic−crystal transition, we propose that the unusual short interatomic contacts mainly arise from the orderly and close packing of $P_4Se_3$ molecules. These findings offer new insights into the intermolecular interactions in 2DIMCs and will highly promote the research and potential applications for 2DIMCs in molecular physics and optoelectronics.

## ■ RESULTS AND DISCUSSION

The $P_4Se_3$ molecule has a cage-like structure, as shown in Figure 1a, the symmetry of which is $C_{3v}$. When $P_4Se_3$ molecules self-assemble into crystals, they are reported to exist in at least four different crystalline phases: two normal room-temperature forms, $\alpha$-$P_4Se_3$ and $\alpha'$-$P_4Se_3$, and two higher temperature plastic crystalline forms, $\beta$-$P_4Se_3$ and $\gamma$-$P_4Se_3$, where the $P_4Se_3$ molecules are arranged in an orderly fashion on the crystal lattice but their orientations are highly disordered.[19−22] The existence of multiple crystalline phases reveals the complexity of intermolecular interactions of $P_4Se_3$ molecules. $\alpha$-$P_4Se_3$ and $\alpha'$-$P_4Se_3$ are both orthorhombic and are in space group *Pnma*, while the latter possesses less efficient packing in the unit cell.[20] The $\alpha$-$P_4Se_3$ single crystals in this work were prepared by a solid-state reaction and further purified with recrystallization from carbon disulfide. Detailed synthetic methods can be found in Materials and Methods in the Supporting Information. The powder X-ray diffraction pattern (Figure S1) of as-synthesized $\alpha$-$P_4Se_3$ crystals clearly demonstrates its high purity and crystallinity, as the sharp diffraction peaks can match well with those of the standard $\alpha$-$P_4Se_3$ (PDF# 74-0811).

$\alpha$-$P_4Se_3$ crystals could be dissolved in a variety of organic solvents, which makes it possible to obtain 2D $\alpha$-$P_4Se_3$ nanoflakes from a solution process.[23−25] Herein, 2D $\alpha$-$P_4Se_3$

nanoflakes were synthesized via a facile drop-casting method with as-synthesized $\alpha$-$P_4Se_3$ crystals as the source. As illustrated in Figure 1b, a drop of $P_4Se_3$ supersaturated solution was placed on a glass substrate inside a covered Petri dish, allowing the carbon disulfide solvent to evaporate naturally. With the gradual volatilization of carbon disulfide, the $P_4Se_3$ molecules could self-assemble into nanoflakes. In particular, it is necessary to vigorously stir the solution before dropping, which promotes the formation of seed crystals.[23] An optical microscopy (OM) image (Figure 1c) of as-synthesized $P_4Se_3$ nanoflakes shows a regular morphology, smooth surface, and large lateral size. The thickness of $P_4Se_3$ nanoflakes was determined by atomic force microscopy (AFM), and the thickness can be as thin as 60 nm (Figure 1d). To identify the crystalline phases and quality of 2D $P_4Se_3$ nanoflakes, Raman spectroscopy was carried out with a laser having a wavelength of 633 nm. The Raman spectrum of $P_4Se_3$ nanoflakes (Figure 1e) shows six internal (intramolecular) modes, which are quite consistent with those of a $\alpha$-$P_4Se_3$ crystal. Molecular vibrations of the six Raman modes can be found in a previous report by Phillips.[26] The spatially resolved Raman mappings in Figure S2 of three typical internal modes at 213, 365, and 485 $cm^{-1}$ suggest the uniformity of the nanoflake. In addition, the external (lattice) modes were also collected, as exhibited in Figure S3. The peak positions of the five low-wavenumber external modes are in accordance with previous reports for $\alpha$-$P_4Se_3$ crystals.[20,27] To identify the chemical composition, energy-dispersive X-ray spectroscopy (EDS) was performed. As shown in Figure S4, the atomic ratio of P and Se is close to 4:3 and the P and Se elements are uniformly distributed in the flake, again confirming the uniformity of the nanoflake. Moreover, the crystallinity, purity, and growth orientation of the 2D $\alpha$-$P_4Se_3$ nanoflakes were further explored with X-ray diffraction (XRD). The seven periodic sharp diffraction peaks shown in Figure 1f can correspond well to the (001) crystal plane of $\alpha$-$P_4Se_3$, which clearly demonstrates the preferred growth orientation, high purity, and quality of as-synthesized 2D $P_4Se_3$ nanoflakes. Because 2D $\alpha$-$P_4Se_3$ nanoflakes are sensitive to moist air (Figure S5), all of the following measurements were carried out under vacuum or in an inert environment.

A more comprehensive and fine analysis of the structure of $P_4Se_3$ flakes was performed by SC-XRD. The crystallographic data and refinement details are presented in Table S1. The cell parameters of 2D $P_4Se_3$ flake are highly in line with the previous reported $\alpha$-$P_4Se_3$.[28,29] Amazingly, a number of unusually short interatomic distances between different molecules were clearly demonstrated (Figure 1g). The four unique short intermolecular Se−Se contacts shown in Figure 3b ranging from 3.63 to 3.81 Å make it possible to describe the structure as a layered lattice with four layers lying orthogonal to the *c* axis per unit cell.[15] The four layers are depicted with different colors in Figure 1g. For instance, the bottom layer is composed of molecules 3, 16, 6, and 5. Between adjacent layers, unusually short intermolecular Se−Se and P−Se contacts were also observed. The Se−Se contacts between molecules 2−8 and 4−14 are 3.78 Å. The P−Se contacts between molecules 2−3 and 6−11 are 3.66 and 3.75 Å, respectively. Since the Pauling−van der Waals radii for Se and P are 200 and 190 pm, respectively, the interatomic distances between Se−Se and P−Se mentioned above are both significantly shorter than the sum of Pauling−van der Waals radii for Se−Se and P−Se: i.e., 400 and 390 pm, respectively.[15,20,30] These unusually short intermolecular interatomic distances actually signify stronger intermolecular interactions than the expected van der Waals force.[10,15,31,32]

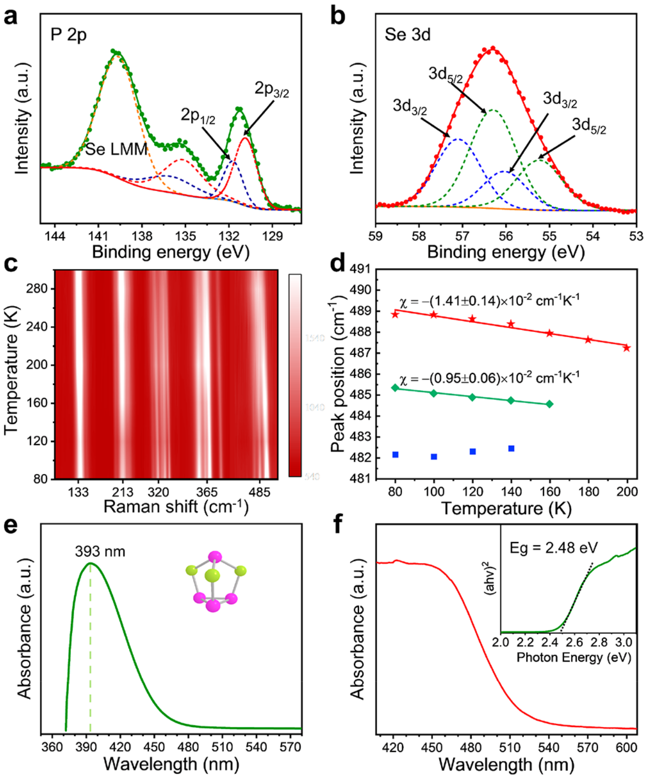

**Figure 2.** Characterization of strong intermolecular interactions in 2D $P_4Se_3$ nanoflakes. (a, b) XPS spectra of P 2p and Se 3d for $P_4Se_3$ nanoflakes, respectively. (c) 2D false-color plot of Raman spectra of 2D $P_4Se_3$ nanoflakes with temperatures ranging from 80 to 300 K. (d) Temperature dependence of Raman peak positions. (e) Absorption spectrum of a dilute solution of $P_4Se_3$ molecules (solvent: carbon disulfide). (f) Absorption spectrum of the $P_4Se_3$ nanoflake and the corresponding Tauc plot.

To further confirm the strong intermolecular interactions between $P_4Se_3$ molecules, the as-synthesized 2D $P_4Se_3$ nanoflakes were characterized by X-ray photoelectron spectroscopy. Figure 2a,b shows the high-resolution X-ray photoelectron spectrum of P 2p and Se 3d, respectively. The fitting peak positions are summarized in Table S2. Though unusually short intermolecular P−Se contacts were observed, the two types of P atoms in the $P_4Se_3$ molecule make it difficult to directly compare the binding energy of P 2p in $P_4Se_3$ with those of other phosphorus compounds. Thus, the binding energies of P $2p_{1/2}$ and P $2p_{3/2}$ are simply determined at 131.71 and 130.84 eV, respectively. However, the three Se atoms in a single $P_4Se_3$ molecule are completely equivalent. In view of the existence of two types of Se atoms (those which deal with strong intermolecular coupling and those which are bonded only within the molecule), it is necessary to employ the four-peak fit to decipher the detected Se 3d line shape.[20,33] Specifically, the relative weights of $3d_{3/2}$ and $3d_{5/2}$ peaks for coupled and noncoupled Se atoms were both set as 2/3, and their binding energy difference was set as 0.8 eV (Table S2).[20,34] At this point, the binding energy of the four peaks can be determined accurately. Eventually the binding energy of Se $3d_{5/2}$ for coupled and noncoupled Se were determined to be

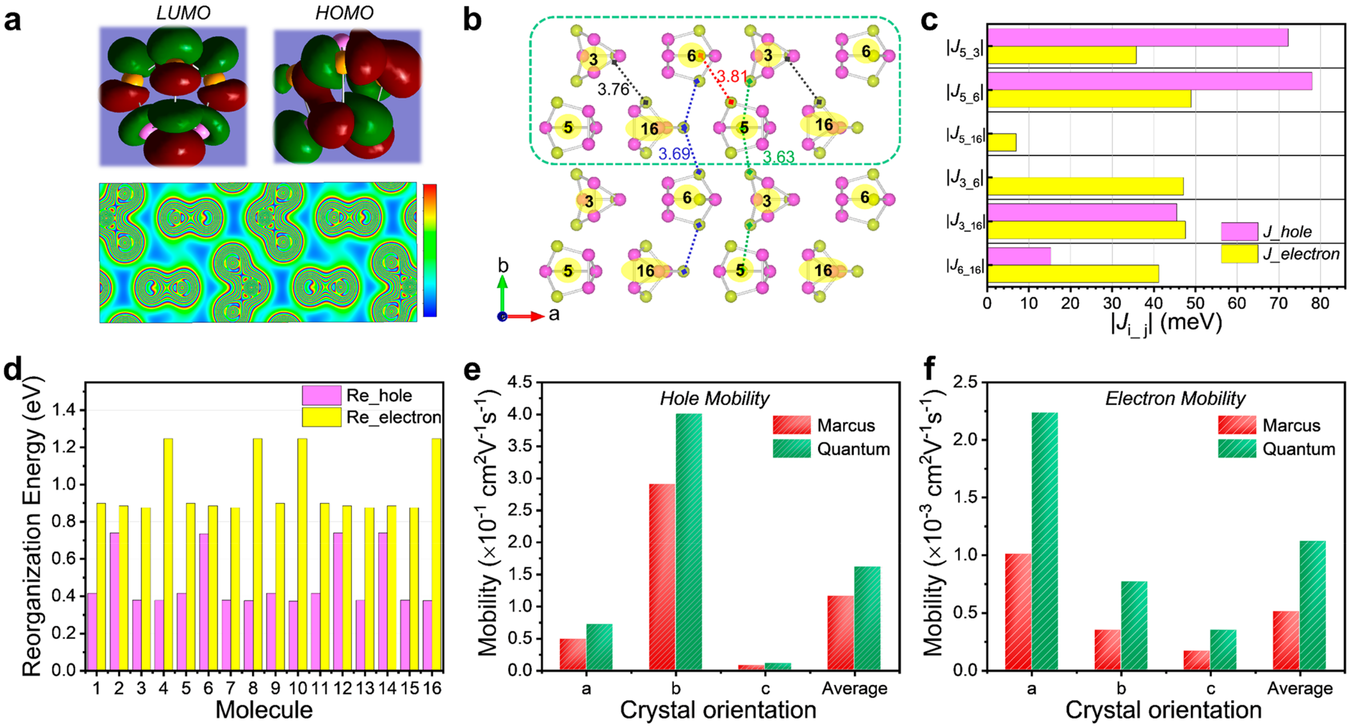

**Figure 3.** Theoretical simulations of intermolecular coupling and charge transport. (a) Calculated LUMO and HOMO orbitals for a single $P_4Se_3$ molecule and total charge density projected on the (001) plane. (b) Crystal structure of the bottom $P_4Se_3$ molecular layer and the unusual short intermolecular Se−Se contacts. (c) Calculated electron and hole transfer integrals for the bottom $P_4Se_3$ molecules. (d) Calculated electron and hole reorganization energies of the 16 $P_4Se_3$ molecules in the unit cell. (e, f) Calculated hole and electron mobilities within the framework of Marcus theory and the quantum nuclear tunneling model, respectively.

56.3 and 55.23 eV, respectively. The binding energy of 3d$_{5/2}$ for coupled Se is slightly higher than those for the Se atoms in CoSe (54.8 eV),[35] $GeSe_2$ (55.3 eV),[34] and $As_2Se_3$ (55.0 eV).[36] Obviously, this phenomenon arises from the unusually short intermolecular Se−Se contacts, which allows electron density to be shared over more atoms.

As a sensitive tool to probe the intermolecular coupling, Raman spectra exhibit a wealth of details for the crystal field. The long-range ordered stacking of inorganic molecules and intermolecular interactions directly lead to the formation of lattice phonons and Davydov-splitting effects.[14,37] At the limit of vanishing intermolecular interactions, the lattice phonons fall into zero frequency and the splits of Raman internal modes (Davydov splitting) disappear.[14] In addition, the first-order temperature coefficient ($\chi$) of Raman modes can effectively reflect the strength of the intermolecular coupling.[38−40] Figure 2c shows the Raman spectra of a $P_4Se_3$ nanoflake at temperatures ranging from 80 to 300 K, and the Raman spectrum under 80 K is displayed in Figure S6a. As the temperature is decreased, the Raman peaks around 320, 365, and 485 cm$^{-1}$ exhibit conspicuous Davydov splitting due to the stronger intermolecular interactions at low temperature. The Raman modes around 320 and 365 cm$^{-1}$ from two and three peaks split into four peaks (Figure S6a,c), respectively. The broad peak at 485 cm$^{-1}$ also splits into three peaks. Though the splitting is usually expected to be small, surprisingly, the Davydov splitting for the $P_4Se_3$ nanoflake is larger than those for the isoelectronic $P_4S_3$ and $As_4S_3$.[15,37,41,42] The notable Davydov splitting reveals the strong intermolecular interactions of $\alpha$-$P_4Se_3$ nanoflakes.[14,15] To further analyze the intermolecular interactions between $P_4Se_3$ molecules, the first-order temperature coefficients ($\chi$) of the Raman modes were extracted (shown in Figure 2d and Figure S6b,c) by fitting the peak position with the equation: $\omega(T) = \omega_0 + \chi T$, where $T$ is the Kelvin temperature of the sample and $\omega_0$ is the Raman frequency with the temperature extrapolated to 0 K.[40,43] As shown in Table S3, the first-order temperature coefficient of $\alpha$-$P_4Se_3$ nanoflakes at 489 cm$^{-1}$ (Figure 2d) is comparable to or slightly larger than those of common 2D van der Waals solids, such as $MoS_2$,[44] $WS_2$,[45] $RhI_3$,[38] and $MnPSe_3$.[46] In addition, in comparison to the previously reported molecular crystal $\beta$-$HgI_2$, the first-order temperature coefficients of $\alpha$-$P_4Se_3$ nanoflakes at 367 and 489 cm$^{-1}$ are both much larger,[39] which confirms the strong intermolecular interactions in 2D $P_4Se_3$ nanoflakes as well.

It has been well established that strong intermolecular coupling can effectively reduce the band gap of molecular crystals due to the effects of static polarization and band dispersion.[47−49] To visually observe the contribution of intermolecular coupling to band-gap re-forming, the absorption spectra of a dilute solution of the inorganic molecule $P_4Se_3$ in $CS_2$ solvent and 2D $P_4Se_3$ nanoflakes were recorded and are presented in Figure 2e,f. The absorption maximum for the dilute solution of $P_4Se_3$ is located at 393 nm, whereas the absorption edge of crystalline $P_4Se_3$ nanoflake is at about 510 nm. The large red shift of light absorption from solution to the crystalline state reveals the strong intermolecular interactions in $\alpha$-$P_4Se_3$ nanoflakes, which leads to the relatively small band gap of 2.48 eV.[15]

In order to obtain a physical image of the strong intermolecular interaction and reveal the relationship between intermolecular coupling and charge transport, detailed theoretical calculations were performed. For a single $P_4Se_3$ molecule, a notable feature is that the HOMO and LUMO orbitals (Figure 3a) are only delocalized on a few atoms rather than the entire molecule, which is significantly different from organic molecules with a conjugated $\pi$-system.[17,50] The HOMO and LUMO energy levels for a single $P_4Se_3$ molecule are determined to be −6.98 and −2.89 eV, respectively; the band gap is obviously larger than the optical gap we measured, again confirming the strong intermolecular interactions in $P_4Se_3$ nanoflakes. To bridge the strong intermolecular coupling and the microstructure, the total charge density distribution was calculated and the top view on the (001) plane is shown in Figure 3a. We found that locations where the intermolecular Se−Se contacts are unusually short possess a higher charge density, which leads to the formation of double-stranded helices along the *a* and *b* axes in each layer. What is more, this double-stranded helix in terms of charge density is an excellent mapping of the $P_4Se_3$ molecule stacking structure (Figure 3b), which reveals the nature of strong intermolecular coupling. Though the microscopic mechanism of strong intermolecular coupling in $P_4Se_3$ nanoflakes has been demonstrated so far, a quantitative analysis of the strength of intermolecular coupling is still lacking. A suitable indicator is the transfer integral calculated according to the overlap of intermolecular orbitals, and it has been used to compare the strength of intermolecular coupling in a great deal of studies.[49,51−54] Thus, the transfer integrals between adjacent $P_4Se_3$ molecules were calculated at the B3LYP/6-311+G** level on the basis of single-crystal stacking and are summarized in Table S4. Figure 3c presents the charge transfer integrals for the bottom-layer $P_4Se_3$ molecules (molecules 3, 16, 6, 5). With molecule 5 as an example, the transfer integral of holes and electrons between molecules 5−3 and 5−6 is larger than that between molecules 5−16. In combination with the molecular stacking in Figure 3b, it can be seen that the unusually short Se−Se contacts play a key role in promoting the intermolecular coupling. Similar conclusions can be drawn from molecules 3, 6, and 16 and from other layers. The transfer integrals for the adjacent $P_4Se_3$ molecules in each layer are displayed in Table S5. In addition, the strength of intermolecular coupling for $P_4Se_3$ molecules between adjacent layers was also analyzed. As exhibited in Tables S6 and S7, the transfer integrals between the different molecules with unusually short Se−Se or P−Se contacts are much larger, such as for the molecules 2−8 and molecules 6−7, which is quite consistent with our anticipation.

Inspired by the strong intermolecular coupling in each layer, we were very interested in exploring the in-plane charge transport of $\alpha$-$P_4Se_3$ nanoflakes, because in-plane charge transport for inorganic molecular crystals has rarely been reported and they have always been regarded as insulating solids.[55−57] Regardless of the transport mechanism, two important molecular parameters governing charge transport are the transfer integral and the reorganization energy ($\lambda$).[58] Therefore, to acquire a rational assessment of the charge transport property in our as-synthesized 2D $P_4Se_3$ nanoflakes, we calculated the reorganization energy of the 16 $P_4Se_3$ molecules in the unit cell, as shown in Figure 3d and Table S8. The reorganization energy of electrons is larger than that of holes, which directly lowers the electron mobility by 2 orders of magnitude in comparison to hole mobility, as exhibited in Figure 3e,f and Table S9. In this work, the mobilities of holes and electrons were calculated by Marcus theory and the quantum nuclear tunneling model. Quantum nuclear tunneling model assumed localized charge, the origin of which could stem from static and/or dynamic disorders or impurity. Since Marcus semiclassical theory usually leads to an underestimation of experimental mobility, we will mainly focus on the mobility calculated by quantum nuclear tunneling model in the following discussion.[59] The hole mobility reaches its maximum value (0.4 $cm^2\ V^{-1}\ s^{-1}$) in the *b*-axis orientation, which is comparable to that of many organic semiconductors and contradicts the viewpoint that the inorganic molecular crystals are insulating solids.[60−62] For the mobility of electrons, the maximum value (0.002 $cm^2\ V^{-1}\ s^{-1}$) is obtained along the *a* axis. Moreover, it can be seen that the in-plane hole and electron mobility is significantly greater than the out-of-plane mobility for 2D $P_4Se_3$ nanoflakes (Figure 3e,f). This phenomenon indicates that the intermolecular coupling within the layers is much stronger than that of adjacent layers, which explains why the $P_4Se_3$ molecules could spontaneously assemble into 2D nanoflakes when the solvent volatilized naturally.

To promote the practical applications of 2D inorganic molecular crystals in optoelectronics and prove the ability of charge transfer in $P_4Se_3$ nanoflakes, we further studied the photoelectric response of the 2D $P_4Se_3$ nanoflakes. The device performance is usually affected by the charge injection. For a good charge injection, the Mott−Schottky barrier on a metal−semiconductor interface is expected to be as small as possoble.[63] Thus, a Kelvin probe force microscope (KPFM) measurement was carried out to acquire the work function of $P_4Se_3$ nanoflakes. As shown in Figure S7a, the potential of the $P_4Se_3$ nanoflake is very close to that of the gold substrate. For convenience, we assume that the Fermi level ($E_f$) of $P_4Se_3$ nanoflakes is equal to the work function of Au. Because the source purity for preparing nanoflakes was high and the whole preparation process was carried out in a glovebox, the 2D $P_4Se_3$ nanoflakes could be regarded as intrinsic semiconductors.[64] In this case, the valence-band maximum (VBM) and conduction-band minimum (CBM) of $P_4Se_3$ nanoflake could be extracted by the equation $E_f - E_{midgap} = \frac{3}{4}kT\ \ln\left(\frac{m_p*}{m_n*}\right)$, where $E_{midgap}$ refers to the midpoint of $E_c$ and $E_v$, $k$ represents the Boltzmann constant, and $m_p$* and $m_n$* are the effective masses of holes and electrons, respectively. When the ratio of effective mass of hole and electron is not particularly large, the value of $\frac{3}{4}kT\ \ln\left(\frac{m_p*}{m_n*}\right)$ is always quite small. For example, the difference of $E_f$ and $E_{midgap}$ is only 0.09 eV at 300 K, when the ratio of effective masses of holes and electrons is 100. Thus, we roughly suppose that $E_f$ is equal to $E_{midgap}$ here. On the basis of the above inferences, the VBM and CBM are estimated to be −6.34 eV and −3.86 eV, respectively, as shown in Figure S7b. To suppressthe Mott−Schottky barrier at metal−$P_4Se_3$ nanoflake interface, we chose silver as the metal electrode. Under the illumination of a 365 nm laser, the current increased monotonically with an increase in the incident optical power (Figure S7c). This result could indicate the dawn of application potentials of 2DIMCs in optoelectronics.

Last but not least, it is highly fascinating that a strong intermolecular interaction can form not only between the different atoms P−Se but also between the same atoms Se−Se. The latter is thought to exist under high-pressure conditions.[32,65] Charge-transfer (CT) theory has been widely used to account for the unusually short intermolecular atom contacts that are formed between different atoms, such as the I···Sb contact in tftib-$SbPh_3$.[6,12,41] Nevertheless, charge-transfer

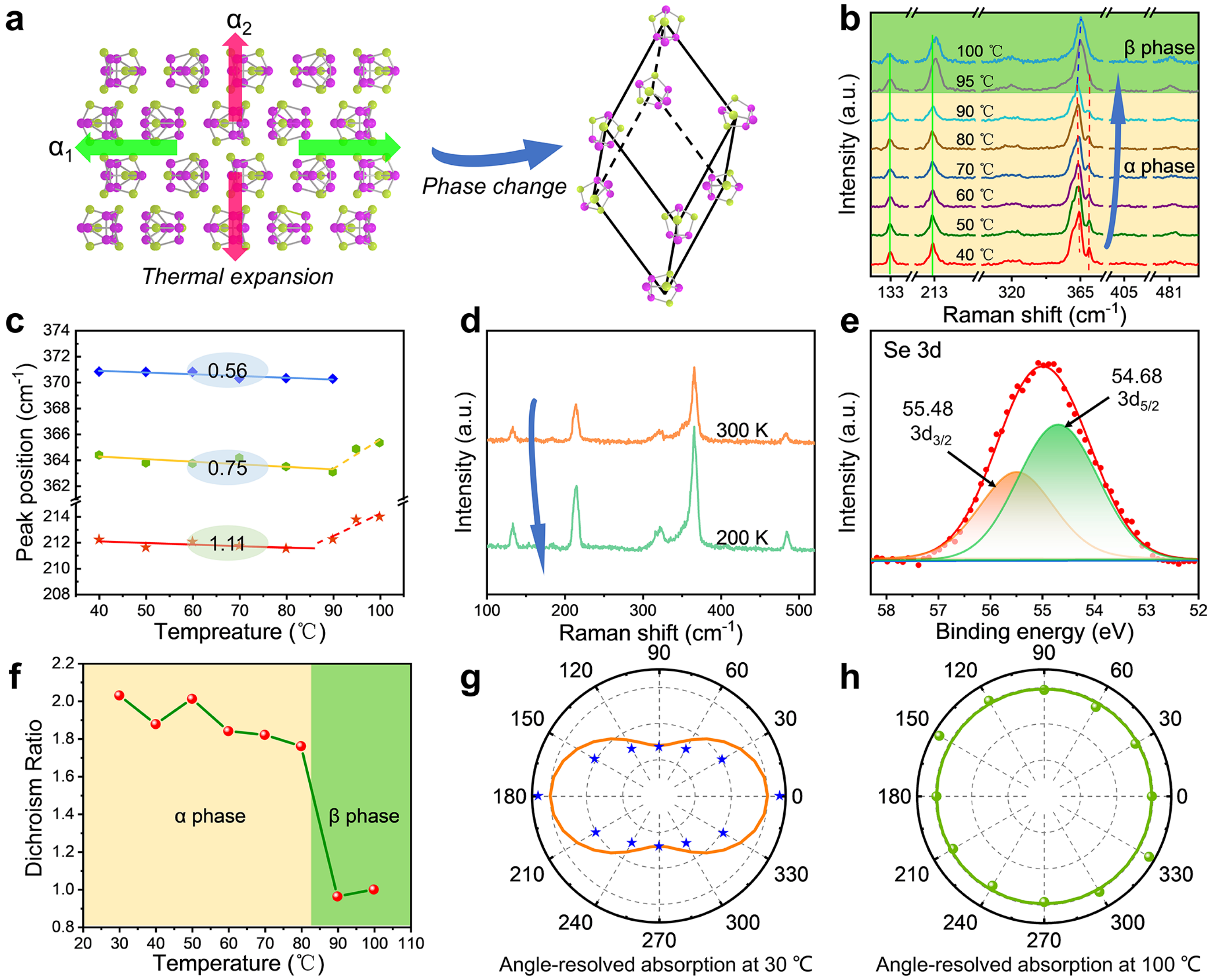

**Figure 4.** Temperature and phase transition dependence of intermolecular coupling. (a) Schematic diagram of thermal expansion and plastic−crystal transition of $\alpha$-$P_4Se_3$ nanoflakes. (b) Temperature-dependent Raman spectra of $\alpha$-$P_4Se_3$ nanoflakes from 40 to 100 °C. (c) Evolution of Raman peak positions with temperature and the ratio ($\theta$) contributed by the explicit term. (d) Raman spectra for the same $P_4Se_3$ nanoflakes cooled to 300 and 200 K. (e) XPS spectrum of Se 3d for the $P_4Se_3$ nanoflake returned to room temperature. (f) *In situ* temperature-dependent dichroism ratio of a $P_4Se_3$ nanoflake. (g, h) Angle-resolved absorption at 450 nm for the $P_4Se_3$ nanoflake at 30 and 100 °C, respectively.

(CT) theory cannot reasonably explain the unusually short intermolecular Se−Se contact in $P_4Se_3$ nanoflakes. Hence, to further figure out the origin of the unusually short intermolecular Se−Se and P−Se contacts, the temperature dependence of intermolecular interactions was studied. During the heating process, the $P_4Se_3$ nanoflakes would undergo two processes, thermal expansion and a plastic−crystal transition (Figure 4a), which provide a wonderful opportunity to investigate the intermolecular coupling.[66] Figure 4b shows the Raman spectra of a $P_4Se_3$ nanoflake in the temperature range from 40 to 100 °C. Before the plastic−crystal transition, the Raman modes at 213, 364, and 371 $cm^{-1}$ exhibited a red shift as the temperature was increased, whereas the Raman mode at 133 $cm^{-1}$ did not show an obvious temperature dependence. The movements of peak positions with temperature for the Raman modes at 213, 364, and 371 $cm^{-1}$ are plotted in Figure 4c. The temperature dependence of the Raman frequency arises from two factors, an "implicit" contribution resulting from concomitant volume change and an "explicit" contribution caused by the temperature effect on a constant-volume crystal.[14] Consequently, the first-order temperature coefficient ($\chi$) of Raman frequency can be further described by $\left(\frac{d\omega}{dT}\right)_P$, with $\left(\frac{d\omega}{dT}\right)_P = \left(\frac{d\omega}{dT}\right)_V - \frac{\alpha}{\beta}\left(\frac{d\omega}{dP}\right)_T$, in which the former term is driven by phonon−phonon interactions (explicit term) and the latter is driven by volume dilation (implicit term).[19,27,67] Here $\alpha$ and $\beta$ are the volume thermal expansion coefficient and compressibility, respectively. Then the portion of the total temperature coefficient arising from the explicit term can be denoted by $\theta$, $\theta = 1 - \left(\frac{dT}{dP}\right)_\omega \left(\frac{\beta}{\alpha}\right)^{-1}$.[27,67] For a molecular solid, if $\theta \approx 0$, then the predominant interaction is an intermolecular van der Waals force, whereas if $\theta \approx 1$, then the principal interaction is a strong covalent bond, which is influenced little by changes in volume. The $\theta$ values calculated by Burns for the Raman modes at 213, 364, and 371 $cm^{-1}$ are presented in Figure 4c.[67] For the Raman modes at 364 and 371 $cm^{-1}$, the $\theta$ values are both located in the range 0−1, which reveals the significant lattice expansion during the heating process.[27] The anomalously large $\theta$ value for the Raman mode at 213 $cm^{-1}$ may result from the strong intra-/intermolecular coupling in $\alpha$-$P_4Se_3$ nanoflakes.[20] Another abnormal phenomenon was that the Davydov splitting between 364 and 371 $cm^{-1}$ increased with an increase in the temperature, and this is because the effect of thermal expansion on Davydov splitting was shadowed by phonon−phonon interactions. When the $P_4Se_3$ nanoflake was heated to 95 °C, the Raman modes at 213 and 364 $cm^{-1}$ suddenly blue shifted and the Raman mode at 371 $cm^{-1}$ stemming from Davydov splitting disappeared, as illustrated in Figure 4b,c. This indicates the occurrence of a phase transition to the orientationally disordered phase $\beta$-$P_4Se_3$.[20] The space group of $\beta$-$P_4Se_3$ is $R3m$, with $a = 1622.3$ pm and $\alpha = 89.47°$.[66] What is more, the thermal expansion and phase transition lead to a decrease in density of about 12%.[21] Next, the temperature was reduced to 300 K and then to 200 K from 100 °C, and the corresponding Raman spectra are displayed in Figure 4d. The Raman mode at 371 $cm^{-1}$ did not reappear with the temperature decreasing, suggesting the plastic−crystal transition is not a reversible process for 2D $\alpha$-$P_4Se_3$, whereas it is actually reversible for the bulk. The irreversible characteristic was further confirmed by the XRD pattern (Figure S8). The disappearance of diffraction peaks can be attributed to the freezing of molecular rotations with a decrease in temperature and incomplete reorientation of disordered $P_4Se_3$ molecules.[68] This made it possible to compare the strengths of intermolecular couplings of $\alpha$-$P_4Se_3$ and $\beta$-$P_4Se_3$. Figure 4e and Figure S9 exhibit the XPS spectrum of Se 3d and P 2p for the $P_4Se_3$ nanoflake after the plastic−crystal transition, respectively. In comparison to the XPS spectra of $\alpha$-$P_4Se_3$ nanoflakes (Figure 2a,b), the binding energies of P and Se both became smaller, which is concrete evidence that the intermolecular coupling is weakened after the phase change. Thus, we conclude that unusually short intermolecular Se−Se and P−Se contacts are caused by an orderly and close packing of $P_4Se_3$ molecules, primarily arising from steric effects produced by the intermolecular repulsive forces.[31]

The processes of thermal expansion and the plastic−crystal transition were further confirmed by the temperature-dependent dichroic ratio in the (001) plane, as displayed in Figure 4f. The dichroic ratio was defined as the absorbance ratio of 0 and 90° at 450 nm (Figure S10), where the direction of the long side of the $P_4Se_3$ nanoflake was fixed at 0°. The large difference in the linear expansion coefficient along the $a$ and $b$ axes allowed us to vary the in-plane dichroism with temperature.[20] Before the plastic−crystal transition, the dichroic ratio gradually decreased from 2.03 to 1.76 with an increase in temperature (Figure 4f and Figure S10). When the plastic−crystal transition occurred, the in-plane dichroism disappeared at the same time, arising from the orientational disorder of $P_4Se_3$ molecules. This shift from in-plane optical anisotropy to isotropy induced by the phase change was further demonstrated by angle-resolved absorption (Figure 4g,h) and polarization-resolved absorption spectra (Figure S11).

## ■ CONCLUSION

In conclusion, we have successfully prepared high-quality 2D $\alpha$-$P_4Se_3$ nanoflakes and revealed the unique short intermolecular Se−Se and P−Se contacts by SC-XRD. The strong intermolecular interaction induced by those contacts was confirmed by XPS, temperature-dependent Raman spectra, and absorption spectra. More importantly, we illustrated the relationship between the strong intermolecular interaction and charge density and demonstrated the significant effects of unusually short interatomic distances on charge transfer integrals on the basis of the results of theoretical calculations. Inspired by the strong intermolecular coupling, we first calculated the in-plane mobility of 2DIMCs with the quantum nuclear tunneling model and demonstrated their photoelectric response. Through an analysis of the thermal expansion and plastic−crystal transition, we proposed that the unusually short interatomic contacts were caused by the orderly and close packing of $P_4Se_3$ molecules. Our work extends the fundamental understanding of intermolecular interactions in 2DIMCs and will greatly promote the research of molecular physics and potential applications of 2DIMCs in electronics and optoelectronics.

## ■ ASSOCIATED CONTENT

### Supporting Information

The Supporting Information is available free of charge at https://pubs.acs.org/doi/10.1021/jacs.1c08030.

> Experimental methods, characterization of bulk $\alpha$-$P_4Se_3$ crystals and 2D $P_4Se_3$ nanoflakes, and detailed theoretical calculations and results (PDF)

## ■ AUTHOR INFORMATION

### Corresponding Authors

**Tianyou Zhai** − *State Key Laboratory of Materials Processing and Die & Mould Technology and School of Materials Science and Engineering, Huazhong University of Science and Technology, Wuhan 430074, People's Republic of China;* orcid.org/0000-0003-0985-4806; Email: zhaity@hust.edu.cn

**Zhigang Shuai** − *MOE Key Laboratory of Organic OptoElectronics and Molecular Engineering, Department of Chemistry, Tsinghua University, Beijing 100084, People's Republic of China;* orcid.org/0000-0003-3867-2331; Email: zgshuai@tsinghua.edu.cn

### Authors

**Xin Feng** − *State Key Laboratory of Materials Processing and Die & Mould Technology and School of Materials Science and Engineering, Huazhong University of Science and Technology, Wuhan 430074, People's Republic of China*

**Xingliang Peng** − *MOE Key Laboratory of Organic OptoElectronics and Molecular Engineering, Department of Chemistry, Tsinghua University, Beijing 100084, People's Republic of China*

**Baixin Peng** − *State Key Laboratory of High Performance Ceramics and Superfine Microstructure, Shanghai Institute of Ceramics, Chinese Academy of Sciences, Shanghai 200050, People's Republic of China*

**Zexin Li** − *State Key Laboratory of Materials Processing and Die & Mould Technology and School of Materials Science and Engineering, Huazhong University of Science and Technology, Wuhan 430074, People's Republic of China*

**Wentao Huang** − *State Key Laboratory of Materials Processing and Die & Mould Technology and School of Materials Science and Engineering, Huazhong University of Science and Technology, Wuhan 430074, People's Republic of China*

**Sijie Yang** − *State Key Laboratory of Materials Processing and Die & Mould Technology and School of Materials Science* *and Engineering, Huazhong University of Science and Technology, Wuhan 430074, People's Republic of China*

**Ke Pei** − *State Key Laboratory of Materials Processing and Die & Mould Technology and School of Materials Science and Engineering, Huazhong University of Science and Technology, Wuhan 430074, People's Republic of China*

**Zongdong Sun** − *State Key Laboratory of Materials Processing and Die & Mould Technology and School of Materials Science and Engineering, Huazhong University of Science and Technology, Wuhan 430074, People's Republic of China*

**Fuqiang Huang** − *State Key Laboratory of High Performance Ceramics and Superfine Microstructure, Shanghai Institute of Ceramics, Chinese Academy of Sciences, Shanghai 200050, People's Republic of China; State Key Laboratory of Rare Earth Materials Chemistry and Applications, College of Chemistry and Molecular Engineering, Peking University, Beijing 100871, People's Republic of China;* orcid.org/0000-0003-0526-5473

**Huiqiao Li** − *State Key Laboratory of Materials Processing and Die & Mould Technology and School of Materials Science and Engineering, Huazhong University of Science and Technology, Wuhan 430074, People's Republic of China;* orcid.org/0000-0001-8114-2542

Complete contact information is available at: https://pubs.acs.org/10.1021/jacs.1c08030

### Author Contributions

⊥X.F. and X.P. contributed equally.

### Notes

The authors declare no competing financial interest.

## ■ ACKNOWLEDGMENTS

This work was supported by the National Natural Science Foundation of China (21825103), the Hubei Provincial Natural Science Foundation of China (2019CFA002), and the Fundamental Research Funds for the Central University (2019kfyXMBZ018). We also acknowledge the technical support from the Analytical and Testing Center at the Huazhong University of Science and Technology.

## ■ REFERENCES

(1) Sakai, N.; Warren, R.; Zhang, F.; Nayak, S.; Liu, J.; Kesava, S. V.; Lin, Y. H.; Biswal, H. S.; Lin, X.; Grovenor, C.; Malinauskas, T.; Basu, A.; Anthopoulos, T. D.; Getautis, V.; Kahn, A.; Riede, M.; Nayak, P. K.; Snaith, H. J. Adduct-based p-doping of organic semiconductors. *Nat. Mater.* **2021**, *20*, 1248−1254.

(2) Luo, Z.; Peng, B.; Zeng, J.; Yu, Z.; Zhao, Y.; Xie, J.; Lan, R.; Ma, Z.; Pan, L.; Cao, K.; Lu, Y.; He, D.; Ning, H.; Meng, W.; Yang, Y.; Chen, X.; Li, W.; Wang, J.; Pan, D.; Tu, X.; Huo, W.; Huang, X.; Shi, D.; Li, L.; Liu, M.; Shi, Y.; Feng, X.; Chan, P. K. L.; Wang, X. Sub-thermionic, ultra-high-gain organic transistors and circuits. *Nat. Commun.* **2021**, *12*, 1928.

(3) Zhong, Y.; Cheng, B.; Park, C.; Ray, A.; Brown, S.; Mujid, F.; Lee, J. U.; Zhou, H.; Suh, J.; Lee, K. H.; Mannix, A. J.; Kang, K.; Sibener, S. J.; Muller, D. A.; Park, J. Wafer-scale synthesis of monolayer two-dimensional porphyrin polymers for hybrid superlattices. *Science* **2019**, *366*, 1379−1384.

(4) Wang, Q.; Yang, F.; Zhang, Y.; Chen, M.; Zhang, X.; Lei, S.; Li, R.; Hu, W. Space-Confined Strategy toward Large-Area Two-Dimensional Single Crystals of Molecular Materials. *J. Am. Chem. Soc.* **2018**, *140*, 5339−5342.

(5) Fratini, S.; Ciuchi, S.; Mayou, D.; de Laissardiere, G. T.; Troisi, A. A map of high-mobility molecular semiconductors. *Nat. Mater.* **2017**, *16*, 998−1002.

(6) Lisac, K.; Topic, F.; Arhangelskis, M.; Cepic, S.; Julien, P. A.; Nickels, C. W.; Morris, A. J.; Friscic, T.; Cincic, D. Halogen-bonded cocrystallization with phosphorus, arsenic and antimony acceptors. *Nat. Commun.* **2019**, *10*, 61.

(7) Bronstein, H.; Nielsen, C. B.; Schroeder, B. C.; McCulloch, I. The role of chemical design in the performance of organic semiconductors. *Nat. Rev. Chem.* **2020**, *4*, 66−77.

(8) Okamoto, T.; Kumagai, S.; Fukuzaki, E.; Ishii, H.; Watanabe, G.; Niitsu, N.; Annaka, T.; Yamagishi, M.; Tani, Y.; Sugiura, H.; Watanabe, T.; Watanabe, S.; Takeya, J. Robust, high-performance n-type organic semiconductors. *Sci. Adv.* **2020**, *6*, No. eaaz0632.

(9) Grimme, S. Do special noncovalent $\pi$-$\pi$ stacking interactions really exist? *Angew. Chem., Int. Ed.* **2008**, *47*, 3430−3434.

(10) Hunter, C. A.; Sanders, J. K. M. The nature of $\pi$-$\pi$ interactions. *J. Am. Chem. Soc.* **1990**, *112*, 5525−5534.

(11) Lin, F.; Jiang, K.; Kaminsky, W.; Zhu, Z.; Jen, A. K. A Nonfullerene Acceptor with Enhanced Intermolecular $\pi$-Core Interaction for High-Performance Organic Solar Cells. *J. Am. Chem. Soc.* **2020**, *142*, 15246−15251.

(12) Dereka, B.; Yu, Q.; Lewis, N. H. C.; Carpenter, W. B.; Bowman, J. M.; Tokmakoff, A. Crossover from hydrogen to chemical bonding. *Science* **2021**, *371*, 160−164.

(13) Wang, B.; Lin, R. B.; Zhang, Z.; Xiang, S.; Chen, B. Hydrogen-Bonded Organic Frameworks as a Tunable Platform for Functional Materials. *J. Am. Chem. Soc.* **2020**, *142*, 14399−14416.

(14) Zallen, R.; Slade, M. L. Influence of pressure and temperature on phonons in molecular chalcogenides: Crystalline $As_4S_4$ and $S_4N_4$. *Phys. Rev. B: Condens. Matter Mater. Phys.* **1978**, *18*, 5775−5798.

(15) Burns, G. R.; Rollo, J. R.; Clark, R. J. H. Raman and resonance Raman studies of tetraphosphorus triselenide. *Inorg. Chem.* **1986**, *25*, 1145−1149.

(16) Han, W.; Huang, P.; Li, L.; Wang, F.; Luo, P.; Liu, K.; Zhou, X.; Li, H.; Zhang, X.; Cui, Y.; Zhai, T. Two-dimensional inorganic molecular crystals. *Nat. Commun.* **2019**, *10*, 4728.

(17) Wang, Y.; Sun, L.; Wang, C.; Yang, F.; Ren, X.; Zhang, X.; Dong, H.; Hu, W. Organic crystalline materials in flexible electronics. *Chem. Soc. Rev.* **2019**, *48*, 1492−1530.

(18) Sun, L.; Wang, Y.; Yang, F.; Zhang, X.; Hu, W. Cocrystal Engineering: A Collaborative Strategy toward Functional Materials. *Adv. Mater.* **2019**, *31*, 1902328.

(19) Burns, G. R. Temperature dependence of the Raman spectrum of tetraphosphorus triselenide. *J. Phys. Chem. Solids* **1986**, *47*, 681−687.

(20) Rollo, J. R.; Burns, G. R.; Robinson, W. T.; Clark, R. J. H.; Dawes, H. M.; Hursthouse, M. B. A new polymorph of tetraphosphorus triselenide, $\alpha'$-$P_4Se_3$: an x-ray, Raman, and XPS study of the normal crystalline phases and a DSC study of the crystalline and the orientationally disordered phases of $P_4Se_3$. *Inorg. Chem.* **1990**, *29*, 2889−2894.

(21) Blachnik, R. The compounds $P_4S_3$, $P_4Se_3$, $As_4S_3$ and $As_4Se_3$ and the quaternary system $P_4S_3$-$P_4Se_3$-$As_4S_3$-$As_4Se_3$. *Thermochim. Acta* **1993**, *213*, 241−259.

(22) Burns, G. R.; Rollo, J. R.; Sarfati, J. D.; Morgan, K. R. Phases of tetraphosphorus triselenide analysed by magic angle spinning $^{31}P$ NMR and Raman spectroscopy, and the Raman spectrum of tetraphosphorus tetraselenide. *Spectrochim. Acta, Part A* **1991**, *47*, 811−818.

(23) Cao, M.; Zhang, C.; Cai, Z.; Xiao, C.; Chen, X.; Yi, K.; Yang, Y.; Lu, Y.; Wei, D. Enhanced photoelectrical response of thermodynamically epitaxial organic crystals at the two-dimensional limit. *Nat. Commun.* **2019**, *10*, 756.

(24) Shi, Y.; Jiang, L.; Liu, J.; Tu, Z.; Hu, Y.; Wu, Q.; Yi, Y.; Gann, E.; McNeill, C. R.; Li, H.; Hu, W.; Zhu, D.; Sirringhaus, H. Bottom-up growth of n-type monolayer molecular crystals on polymeric substrate for optoelectronic device applications. *Nat. Commun.* **2018**, *9*, 2933.

(25) Jiang, L.; Dong, H.; Meng, Q.; Li, H.; He, M.; Wei, Z.; He, Y.; Hu, W. Millimeter-sized molecular monolayer two-dimensional crystals. *Adv. Mater.* **2011**, *23*, 2059−2063.

(26) Phillips, R. T.; Wolverson, D.; Burdis, M. S.; Fang, Y. Observation of discrete molecular structures in glassy $P_xSe_{1-x}$ by Raman spectroscopy. *Phys. Rev. Lett.* **1989**, *63*, 2574−2577.

(27) Burns, G. R.; Clark, R. J. H. Pressure dependence of the Raman spectrum of crystalline tetraphosphorus triselenide. *J. Phys. Chem. Solids* **1986**, *47*, 1049−1055.

(28) Keulen, E.; Vos, A. The crystal structure of $P_4Se_3$. *Acta Crystallogr.* **1959**, *12*, 323−329.

(29) Weis, P.; Hettich, C.; Kratzert, D.; Krossing, I. Homoleptic Silver Complexes of the Cages $P_4Se_3$ and $As_4S_3$. *Eur. J. Inorg. Chem.* **2019**, *2019*, 1657−1668.

(30) Bougeard, D. Lattice dynamics and intermolecular forces in $P_4Se_3$ derived from the Raman spectra. *J. Raman Spectrosc.* **1989**, *20*, 605−608.

(31) Chandler, D.; Weeks, J. D.; Andersen, H. C. Van der waals picture of liquids, solids, and phase transformations. *Science* **1983**, *220*, 787−794.

(32) Batsanov, S. S. Van der Waals Radii of Elements. *Inorg. Mater.* **2001**, *37*, 871−885.

(33) Wei, D.; Yin, J.; Ju, Z.; Zeng, S.; Li, H.; Zhao, W.; Wei, Y.; Li, H. Cage-like $P_4S_3$ molecule as promising anode with high capacity and cycling stability for $Li^+/Na^+/K^+$ storage. *J. Energy Chem.* **2020**, *50*, 187−194.

(34) Kandil, K. M.; Kotkata, M. F.; Theye, M. L.; Gheorghiu, A.; Senemaud, C.; Dixmier, J. Chemical and structural studies of disorder and defects in a-$GeSe_2$ films as a function of thermal annealing. *Phys. Rev. B: Condens. Matter Mater. Phys.* **1995**, *51*, 17565−17573.

(35) Shenasa, M.; Sainkar, S.; Lichtman, D. XPS study of some selected selenium compounds. *J. Electron Spectrosc. Relat. Phenom.* **1986**, *40*, 329−337.

(36) Sarode, P. R.; Rao, K. J.; Hegde, M. S.; Rao, C. N. R. Study of $As_2(Se,Te)_3$ glasses by X-ray absorption and photoelectron spectroscopy. *J. Phys. C: Solid State Phys.* **1979**, *12*, 4119−4128.

(37) Chattopadhyay, T.; Carlone, C.; Jayaraman, A.; Schnering, H. G. v. Temperature and pressure dependence of the Raman spectrum of crystalline $P_4S_3$. *Phys. Rev. B: Condens. Matter Mater. Phys.* **1981**, *23*, 2471−2483.

(38) Wang, F.; Zhang, Z.; Zhang, Y.; Nie, A.; Zhao, W.; Wang, D.; Huang, F.; Zhai, T. Honeycomb $RhI_3$ Flakes with High Environmental Stability for Optoelectronics. *Adv. Mater.* **2020**, *32*, 2001979.

(39) Lin, Z.; Ding, Y.; Zheng, W.; Zhu, Y.; Zhu, S.; Huang, F. 2D van der Waals Molecular Crystal $\beta$-$HgI_2$: Economical, Rapid, and Substrate-Free Liquid-Phase Synthesis and Strong In-Plane Optical Anisotropy. *Small* **2021**, *17*, 2005368.

(40) Taube, A.; Apiska, A.; Judek, J.; Zdrojek, M. Temperature dependence of Raman shifts in layered $ReSe_2$ and $SnSe_2$ semiconductor nanosheets. *Appl. Phys. Lett.* **2015**, *107*, 013105.

(41) Fernando, W. S. Single crystal Raman spectra of $SbI_3\cdot 3S_8$; $CHI_3\cdot 3S_8$ and $AsI_3\cdot 3S_8$. *J. Inorg. Nucl. Chem.* **1981**, *43*, 1141−1145.

(42) Chattopadhyay, T.; Carlone, C.; Jayaraman, A.; Schnering, H. G. v. Effect of temperature and pressure on the raman spectrum of $As_4S_3$. *J. Phys. Chem. Solids* **1982**, *43*, 277−284.

(43) Late, D. J.; Shirodkar, S. N.; Waghmare, U. V.; Dravid, V. P.; Rao, C. N. R. Thermal Expansion, Anharmonicity and Temperature-Dependent Raman Spectra of Single- and Few-Layer $MoSe_2$ and $WSe_2$. *ChemPhysChem* **2014**, *15*, 1592−1598.

(44) Sahoo, S.; Gaur, A. P. S.; Ahmadi, M.; Guinel, M. J. F.; Katiyar, R. S. Temperature-Dependent Raman Studies and Thermal Conductivity of Few-Layer $MoS_2$. *J. Phys. Chem. C* **2013**, *117*, 9042−9047.

(45) Peimyoo, N.; Shang, J.; Yang, W.; Wang, Y.; Cong, C.; Yu, T. Thermal conductivity determination of suspended mono- and bilayer $WS_2$ by Raman spectroscopy. *Nano Res.* **2015**, *8*, 1210−1221.

(46) Liu, G.; Su, J.; Feng, X.; Li, H.; Zhai, T. Synthesis of 2D ternary layered manganese phosphorous trichalcogenides towards ultraviolet photodetection. *Sci. China Mater.* **2021**, *64*, 2251−2260.

(47) Yamada, K.; Yanagisawa, S.; Koganezawa, T.; Mase, K.; Sato, N.; Yoshida, H. Impact of the molecular quadrupole moment on ionization energy and electron affinity of organic thin films: Experimental determination of electrostatic potential and electronic polarization energies. *Phys. Rev. B: Condens. Matter Mater. Phys.* **2018**, *97*, 245206.

(48) Sharifzadeh, S.; Biller, A.; Kronik, L.; Neaton, J. B. Quasiparticle and optical spectroscopy of the organic semiconductors pentacene and PTCDA from first principles. *Phys. Rev. B: Condens. Matter Mater. Phys.* **2012**, *85*, 125307.

(49) McGarry, K. A.; Xie, W.; Sutton, C.; Risko, C.; Wu, Y.; Young, V. G.; Brédas, J.-L.; Frisbie, C. D.; Douglas, C. J. Rubrene-Based Single-Crystal Organic Semiconductors: Synthesis, Electronic Structure, and Charge-Transport Properties. *Chem. Mater.* **2013**, *25*, 2254−2263.

(50) Coropceanu, V.; Cornil, J.; da Silva Filho, D. A.; Olivier, Y.; Silbey, R.; Bredas, J. L. Charge transport in organic semiconductors. *Chem. Rev.* **2007**, *107*, 926−952.

(51) Sosorev, A. Y. Simple charge transport model for efficient search of high-mobility organic semiconductor crystals. *Mater. Des.* **2020**, *192*, 108730.

(52) Fratini, S.; Nikolka, M.; Salleo, A.; Schweicher, G.; Sirringhaus, H. Charge transport in high-mobility conjugated polymers and molecular semiconductors. *Nat. Mater.* **2020**, *19*, 491−502.

(53) Schweicher, G.; D'Avino, G.; Ruggiero, M. T.; Harkin, D. J.; Broch, K.; Venkateshvaran, D.; Liu, G.; Richard, A.; Ruzie, C.; Armstrong, J.; Kennedy, A. R.; Shankland, K.; Takimiya, K.; Geerts, Y. H.; Zeitler, J. A.; Fratini, S.; Sirringhaus, H. Chasing the "Killer" Phonon Mode for the Rational Design of Low-Disorder, High-Mobility Molecular Semiconductors. *Adv. Mater.* **2019**, *31*, 1902407.

(54) Peng, X.; Li, Q.; Shuai, Z. Influences of dynamic and static disorder on the carrier mobility of BTBT-C12 derivatives: a multiscale computational study. *Nanoscale* **2021**, *13*, 3252−3262.

(55) Reucroft, P. J.; Kronick, P. L.; Scott, H.; Labes, M. M. Some Cases of Apparent High Conductivity in Simple Molecular Crystals. *Nature* **1964**, *201*, 609−609.

(56) Adams, A. R.; Spear, W. E. The charge transport in orthorhombic sulphur crystals. *J. Phys. Chem. Solids* **1964**, *25*, 1113−1118.

(57) Street, G. B.; Gill, W. D. Photoconductivity and drift mobilities in single crystal realgar ($As_4S_4$). *Phys. Status Solidi B* **1966**, *18*, 601−607.

(58) Tan, Y.; Casetti, N. C.; Boudouris, B. W.; Savoie, B. M. Molecular Design Features for Charge Transport in Nonconjugated Radical Polymers. *J. Am. Chem. Soc.* **2021**, *143*, 11994−12002.

(59) Shuai, Z.; Li, W.; Ren, J.; Jiang, Y.; Geng, H. Applying Marcus theory to describe the carrier transports in organic semiconductors: Limitations and beyond. *J. Chem. Phys.* **2020**, *153*, 080902.

(60) He, T.; Zhang, X.; Jia, J.; Li, Y.; Tao, X. Three-dimensional charge transport in organic semiconductor single crystals. *Adv. Mater.* **2012**, *24*, 2171−2175.

(61) Shi, Y. R.; Wei, H. L.; Jia, X. B.; Liu, Y. F. Effects of crystal structures and intermolecular interactions on charge transport properties of organic semiconductors. *J. Mater. Sci.* **2018**, *53*, 15569−15587.

(62) Ji, D.; Li, T.; Liu, J.; Amirjalayer, S.; Zhong, M.; Zhang, Z. Y.; Huang, X.; Wei, Z.; Dong, H.; Hu, W.; Fuchs, H. Band-like transport in small-molecule thin films toward high mobility and ultrahigh detectivity phototransistor arrays. *Nat. Commun.* **2019**, *10*, 12.

(63) Bürgi, L.; Richards, T. J.; Friend, R. H.; Sirringhaus, H. Close look at charge carrier injection in polymer field-effect transistors. *J. Appl. Phys.* **2003**, *94*, 6129−6137.

(64) Zaumseil, J.; Sirringhaus, H. Electron and ambipolar transport in organic field-effect transistors. *Chem. Rev.* **2007**, *107*, 1296−1323.

(65) Pereira, A. L. J.; Gracia, L.; Santamaría-Pérez, D.; Vilaplana, R.; Manjón, F. J.; Errandonea, D.; Nalin, M.; Beltrán, A. Structural and vibrational study of cubic $Sb_2O_3$ under high pressure. *Phys. Rev. B: Condens. Matter Mater. Phys.* **2012**, *85*, 174108.

(66) Blachnik, R.; Wickel, U. Thermal behaviour of $A_4B_3$ cage molecules (A = P, As; B = S, Se). *Thermochim. Acta* **1984**, *81*, 185−196.

(67) Burns, G. R.; Rollo, J. R. The use of Raman spectroscopy as a probe for the intermolecular bonding in crystalline tetraphosphorus trisulphide. *J. Phys. Chem. Solids* **1987**, *48*, 347−354.

(68) Das, S.; Mondal, A.; Reddy, C. M. Harnessing molecular rotations in plastic crystals: a holistic view for crystal engineering of adaptive soft materials. *Chem. Soc. Rev.* **2020**, *49*, 8878−8896.

https://doi.org/10.1021/jacs.1c08030